Tracking the Spatio-Temporal Evolution of Foreshocks Preceding the Mw 6.1 2009 L'Aquila Earthquake

Leoncio Cabrera, Piero Poli, William B. Frank

JGR Solid Earth

RESEARCH ARTICLE
10.1029/2021JB023888

Tracking the Spatio-Temporal Evolution of Foreshocks Preceding the Mw 6.1 2009 L'Aquila Earthquake

Leoncio Cabrera[1], Piero Poli[1], and William B. Frank[2]

[1]ISTerre Institut des Sciences de la Terre, CNRS, Université Grenoble Alpes, Grenoble, France, [2]Department of Earth, Atmospheric and Planetary Sciences, Massachusetts Institute of Technology, Cambridge, MA, USA

Key Points:

- We build a dense, high-resolution catalog of foreshocks before the M6.1 L'Aquila earthquake
- Our catalog captures a complex two-stage evolution of precursory seismicity
- We interpret that the precursory seismicity is driven by aseismic slip and stress interactions between earthquakes

Supporting Information:

Supporting Information may be found in the online version of this article.

Correspondence to:

L. Cabrera,
leoncio.cabrera@univ-grenoble-alpes.fr

Citation:

Cabrera, L., Poli, P., & Frank, W. B. (2022). Tracking the spatio-temporal evolution of foreshocks preceding the Mw 6.1 2009 L'Aquila earthquake. *Journal of Geophysical Research: Solid Earth*, *127*, e2021JB023888. https://doi.org/10.1029/2021JB023888

Received 22 DEC 2021
Accepted 27 FEB 2022

Abstract How faulting processes lead to a large earthquake is a fundamental question in seismology. To better constrain this pre-seismic stage, we create a dense seismic catalog via template matching to analyze the precursory phase of the Mw 6.1 L'Aquila earthquake that occurred in central Italy in 2009. We estimate several physical parameters in time, such as the coefficient of variation, the seismic moment release, the effective stress drop, and analyze spatio-temporal patterns to study the evolution of the sequence and the earthquake interactions. We observe that the precursory phase experiences multiple accelerations of the seismicity rate that we divide into two main sequences with different signatures and features: the first part exhibits weak earthquake interactions, quasi-continuous moment release, slow spatial migration patterns, and a lower effective stress drop, pointing to aseismic processes. The second sequence exhibits strong temporal clustering, fast seismicity expansion, and a larger effective stress drop typical of a stress transfer process. We interpret the differences in seismicity behaviors between the two sequences as distinct physical mechanisms that are controlled by different physical properties of the fault system. We conclude that the L'Aquila earthquake is preceded by a complex preparation, made up of different physical processes over different time scales on faults with different physical properties.

Plain Language Summary In this work, we study the seismicity before the Mw 6.1 2009 L'Aquila earthquake. We first catalog nearly 5000 events from the continuous seismic record. We then analyze the spatio-temporal evolution of this sequence with several physical parameters. We observe that the sequence is divided into two main sequences. Our results indicate that several different physical mechanisms (e.g., aseismic deformation, stress transfer due to earthquake interactions) and potential heterogeneities in the fault system (e.g., the distance between seismic regions) controlled how the earthquake sequence played out. Our observations show a complex spatiotemporal evolution during the precursory phase and challenge classic fault models that explain earthquake initiation as a process along a homogenous planar fault.

1. Introduction

The characterization of the physical processes occurring before major earthquakes is an essential step towards understanding when and where future earthquakes will nucleate. So far, physical models have been proposed to explain the processes that lead to large seismic events, including cascade, pre-slip, and progressive or migratory localization (Ellsworth & Beroza, 1995; Kato & Ben-Zion, 2020; McLaskey, 2019). Which one of these mechanisms best represents the physics of the precursory phase of earthquakes is still under debate.

One of the most powerful observational tools to study the physical processes of earthquake nucleation are foreshocks, small earthquakes that precede some large mainshocks (Bouchon et al., 2013; Dodge et al., 1996). Foreshocks were first observed more than a century ago (Omori, 1908). Since then, many laboratory studies have focused on the precursory moment release (Acosta et al., 2019), aseismic slip and stress changes (McLaskey & Kilgore, 2013; McLaskey & Lockner, 2014), and other characteristics of the foreshocks during the initiation of laboratory earthquakes (McLaskey, 2019 and references therein). In addition, direct seismological observations in different seismotectonic settings such as strike-slip faults (e.g., Bouchon et al., 2011; Chen & Shearer, 2013; Dodge et al., 1996, 1995; Durand et al., 2020; Ellsworth & Bulut, 2018; Shelly, 2020; Tape et al., 2018; Yoon et al., 2019), subduction zones (Bouchon et al., 2013; Kato et al., 2012; Ruiz et al., 2014, 2017), and extensional regimes (Sánchez-Reyes et al., 2021; Sugan et al., 2014) have been carried out to assess which model best explains the occurrence of foreshocks and the physical processes occurring during the precursory phase of large earthquakes. More recently, some studies have taken advantage of high-resolution detection methods, such as

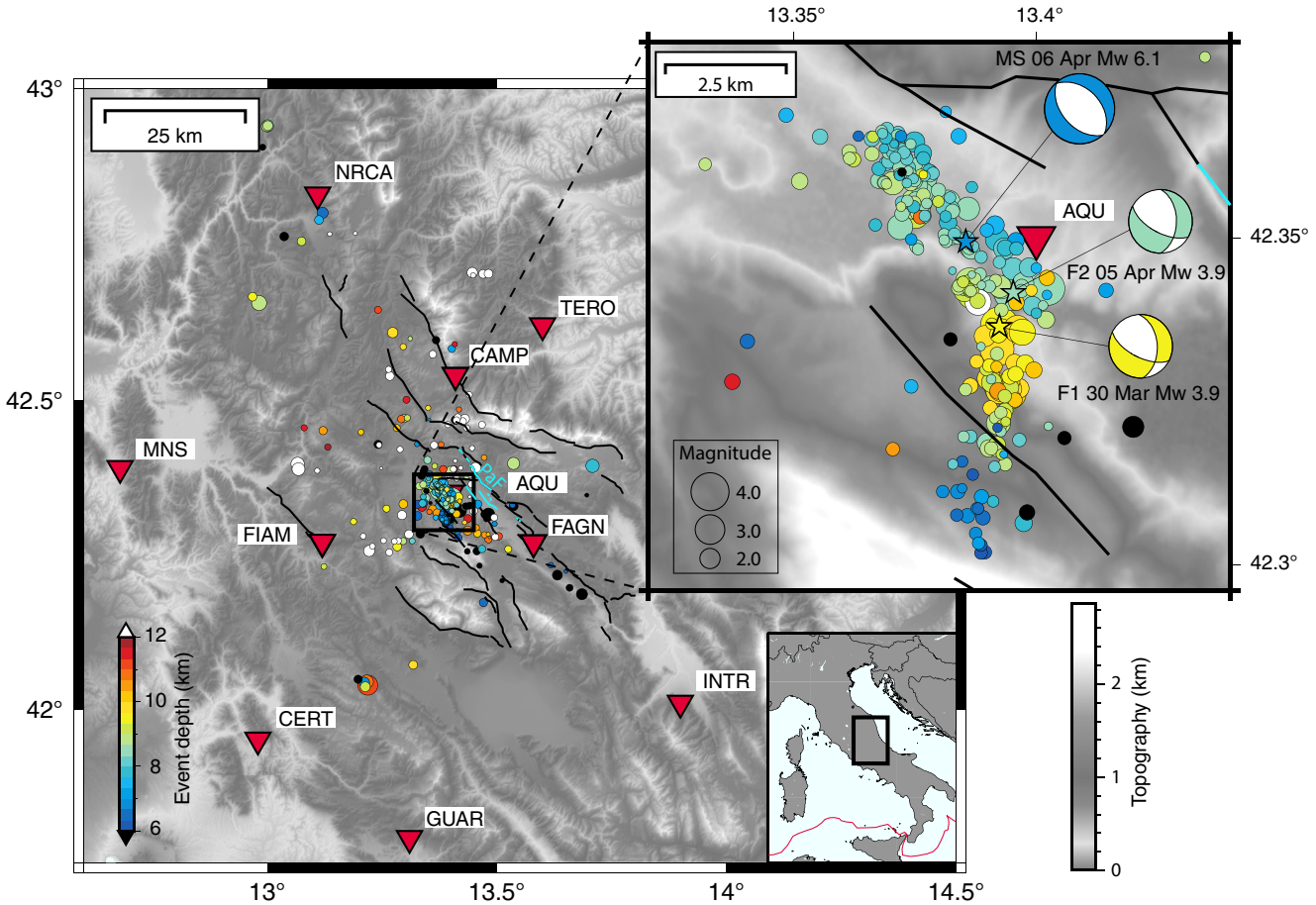

Figure 1. Location map for the L'Aquila earthquake showing the precursory seismicity detected by Chiaraluce, Valoroso, et al. (2011); our 267 template events are drawn from this earthquake catalog and are shown in the zoomed map. The broadband stations we analyzed are shown by the red triangles. Black and cyan thin lines respectively represent traces of the active mapped faults and co-seismic surface ruptures, respectively (Boncio et al., 2010). PaF indicates the location of the Paganica Fault. Upper-right zoom: 267 events used as templates to scan continuous data. Their color and size are respectively coded to depth and magnitude. Beachballs (compressional quadrants in colors) represent source mechanisms (reported by INGV) for the mainshock (MS 6 April) and the two foreshocks Mw 3.9 1 week (F1 30 March) and 5 h (F2 5 April) before it. All of them correspond to normal (extensional) mechanisms.

template matching and/or machine learning (e.g., Durand et al., 2020; Gardonio et al., 2019; Ross et al., 2019; Sánchez-Reyes et al., 2021; Shelly, 2020; Yoon et al., 2019), and the availability of better field data (i.e., more stations near faults; e.g., Meng & Fan [2021]; Savage et al. [2017]; Simon et al. [2021]; Tape et al. [2018]) to study foreshocks. These studies reveal an increased spatiotemporal complexity (i.e., fault interactions, volumetric processes, heterogeneous fault properties) of the processes taking place before large earthquakes. This complexity, mainly revealed by foreshocks patterns, is hard to reconcile with a single physical explanation of the precursory phase (cascade or pre-slip). In addition, the observed foreshocks patterns challenge the actual laboratory scale and theoretical models, which treat earthquake initiation as a process along a homogenous planar fault (Dieterich, 1992; Liu & Rice, 2005; Marone, 1998; Rubin & Ampuero, 2005) or a combination of several planar fault segments (Shimizu et al., 2021), although some cases with non-planar fault geometry exist (e.g., Dutta et al., 2021; Zhang et al., 2014).

To gain insight into the ongoing physical processes occurring near the nucleation region before a large earthquake, we study the Mw 6.1 2009 L'Aquila earthquake and its foreshock sequence. This event, which struck central Italy on 6 April 2009 (01:32 UTC) and caused damage and fatalities, was preceded by more than 500 small ($M > 0.5$) earthquakes since the beginning of January (Chiaraluce, Valoroso, et al., 2011). Based on the locations of the events, Chiaraluce, Valoroso, et al. (2011) reported that the sequence of foreshocks took place in two different faults: (a) the main fault, where the mainshock (Figure 1) occurs on 6 April 2009, that hosts most of the seismicity

occurring from the beginning of January until 30 March and (b) an antithetic fault that is activated by an Mw 3.9 foreshock (hereafter F1, Figure 1) on 30 March 2009. On 5 April 2009 (5 h before the mainshock), the seismicity migrates back to the main fault after the occurrence of another Mw 3.9 foreshock (hereafter F2, Figure 1, Chiaraluce, Valoroso, et al., 2011). The co-seismic rupture took place in the Paganica fault (Cheloni et al., 2010; Falcucci et al., 2009; labeled PaF in Figure 1), generating exposed ground deformation (Boncio et al., 2010; Falcucci et al., 2009) and maximum surface displacements of 8.1 and 16.5 cm in the vertical and horizontal directions, respectively (Cheloni et al., 2010). Joint inversion using GPS, strong motion, and Synthetic Aperture Radar (SAR) data indicate that the maximum slip on the fault is about 1.4 m (Cirella et al., 2012). According to different rupture models (e.g., Cheloni et al., 2010; Cirella et al., 2009, 2012; Scognamiglio et al., 2010), the slip was concentrated in two main asperities: a small patch updip from the hypocenter, and a second, larger asperity located to the southeast along strike. In this context, the foreshocks were located at the base of the activated fault plane in a region where almost no slip occurred during the mainshock rupture (Valoroso et al., 2013).

Here, we complement previous studies of foreshocks of the L'Aquila earthquake (Chiaraluce, Valoroso, et al., 2011; Sugan et al., 2014; Valoroso et al., 2013; Vuan et al., 2018) by estimating quantitative parameters of the spatiotemporal evolution of the foreshocks sequence. We focus on an area of 10 × 10 km surrounding the epicenter (Figure 1). We densify the catalog of seismicity before the L'Aquila earthquake by using template matching (Gibbons & Ringdal, 2006) to scan 6 months of data before the main shock. We use a frequency band between 5 and 30 Hz. The inclusion of high frequencies (>20 Hz) compared to previous studies (Sugan et al., 2014; Vuan et al., 2018) permitted us to detect more small events ($\sim M < 1.0$), which are best captured at high frequency. Our final catalog with coverage from 6 October 2008–6 April 2009 contains 4978 events; the first event occurring on 3 January 2009. No seismicity was detected from 6 October 2008–2 January 2009.

Using this new catalog, we analyze the seismic sequence of foreshocks by tracking the time evolution of temporal clustering (earthquake interactions), seismic moment release, and effective stress drop. We also study the spatio-temporal evolution of the events to better characterize the precursory phase of the L'Aquila earthquake. Based on these results, we discuss the physical mechanisms that control the foreshock sequence, ultimately leading to the mainshock.

2. Extending the Seismic Catalog

We apply template matching (Gibbons & Ringdal, 2006) to continuous seismic data collected by the Istituto Nazionale di Geofisica e Vulcanologia (INGV) from 6 October 2008–6 April 2009 (6 months). We use 10 broadband three-component stations (red triangles in Figure 1) from the Italian Seismic Network (INGV Seismological Data Center., 2006) and the Mediterranean Very Broadband Seismographic Network (MedNet Project Partner Institutions, 1990). Data were continuously recorded at a sampling rate of 100 Hz. Before using the data to study earthquakes, we performed a visual inspection of the spectrograms (Figure S1 in Supporting Information S1) to find the frequency range that is the least affected by the strong anthropogenic noise in the Apennines (Poli et al., 2020). We choose to filter the continuous data from 5 to 30 Hz after this analysis. The dataset was then organized into 24-hr continuous files with all gaps filled with zeros.

We consider 512 foreshocks reported by Chiaraluce, Valoroso, et al. (2011) as potential templates, which have relative horizontal and vertical location errors about 40 and 80 m, respectively (Chiaraluce, Valoroso, et al., 2011). We identify the highest-quality events by estimating the signal-to-noise ratio (SNR) of each event as the ratio between the RMS velocity during the first 3 s of the P and S waves (for vertical and horizontal components, respectively), and the RMS velocity during a 3 s of noise before the P and S wave arrival times (e.g., Cabrera et al., 2021; Frank et al., 2017). We estimate the arrivals using 1D velocity models for P (Chiaraluce, Chiarabba, et al., 2011) and S waves (Herrmann et al., 2011). A signal is retained as a final template if it has a SNR ≥ 2 for at least 12 components. We finally retained 267 template event waveforms (inset in Figure 1), defined as the 3.5 s time windows that start 0.5 s before the P- and S-wave arrivals at each station for the vertical and horizontal components, respectively, and filtered in an identical manner to the continuous data (bandpassed between 5 and 30 Hz). The template waveforms are then correlated against a sliding window of continuous data using a GPU-architecture and the Fast Matched Filter algorithm (Beaucé et al., 2018) to obtain daily correlation functions. We search sample-by-sample considering a detection threshold of 12 times the median absolute deviation (MAD) of the correlation function averaged over all stations and channels to detect events significantly similar

to the template. We defined this detection threshold to minimize false detections by first scanning the continuous data using the templates flipped in time (see an example in Figure S2 in Supporting Information S1). With this approach, the data are scanned using non-physical and acausal templates unlikely to detect anything, but with the same frequency content as the original templates. We test the number of detections using NxMAD with N in the range 9–12 (see Figure S3 in Supporting Information S1), and we decided to use $N = 12$ as this threshold provides only one false detection during the whole period of time (6 October 2008–6 April 2009). To remove double detections over the same time window, we merge consecutive detections with differential times less than 4 s; we keep the detection with the highest network-averaged correlation coefficient as the final detection.

We estimate the magnitude of each new event by computing the mean P- and S-wave amplitude ratio between the template event and the detection over the components with a SNR ≥ 2. Using the template event's catalog magnitude as a reference, the magnitude of a detected event is determined, assuming that a ratio of 10 of the amplitude ratio corresponds to a variation of one unit of magnitude (e.g., Cabrera et al., 2021; Frank et al., 2017; Peng & Zhao, 2009).

We further attempt to relocate the newly detected seismicity with respect to the templates. For this scope, we use pair-wise cross-correlation (CC) between each template and its detections to measure differential delay times. For each event pair, we use waveform windows of 2 s starting 1 s before the phase arrival for both P- and S-waves. We then relocate each family of detections (a template and its detections) with GrowClust (Trugman & Shearer, 2017). An event pair is only used if its cross-correlation coefficient ($rmin$) is $\geq$0.6 with a maximum source-receiver distance ($delmax$) of 80 km. We also considered a maximum root-mean-square differential time residual ($rmsmax$) ≤ 0.2 for a proposed cluster merger to be allowed during relocation (see Trugman & Shearer, 2017 for more details). This procedure resulted in 722 relocated events or ~17% of the original catalog (Figure S4 in Supporting Information S1). Although low, this percentage is not surprising given the configuration of the network. For example, Ross et al. (2019) relocated 38.7% of events using a denser array of stations in California, and Simon et al. (2021) relocated 11.6% of their catalog in Switzerland, in both cases after template matching. This data reduction is because double difference relocations rely on high quality correlations at a single station, while template matching leverages an average correlation across the entire network to identify events that would otherwise go unnoticed. This means that some events that could be detected by template matching can have relatively low correlation coefficients that are not necessarily suitable for relocation. Although it is possible to increase the number of relocated events by relaxing some parameters like the minimum cross-correlation coefficient $rmsmax$, we preferred to use parameter values similar to previous works (e.g., Ross et al., 2019; Trugman & Shearer, 2017) to prevent degradation of the relocation quality.

As only a small number of events can be relocated with the approach described above, we consider the newly detected to have occurred at the same hypocenter (determined by Chiaraluce, Valoroso, et al. [2011]) as the template. We estimated the distance between the initial location of the detections and the relocated position of new detections. On average, horizontal and vertical distances between templates and new detections are in the order of 83 and 66 m, respectively (see Figure S5-6 in Supporting Information S1). These values are similar to other studies (~100–200 m, Ross et al. [2019]; Simon et al. [2021]).

Our final catalog contains 4978 events with magnitude ranging from −0.4 to 3.9 (Figure 2). We estimate the magnitude of completeness (Mc) of our catalog, using the Lillefors test implemented by Herrmann and Marzocchi (2021), which in general provides conservative values of the Mc (see examples in Herrmann & Marzocchi [2021]) and allows us to ensure the stability of our later analysis. We use a binning of $\Delta M = 0.01$; we also test Mc for two significance levels of $\alpha = 0.05$ and $\alpha = 0.1$, obtaining Mc = 0.8 and Mc = 0.9, respectively. As indicated by Herrmann and Marzocchi (2021), choosing $\alpha = 0.1$ is conservative in a statistical sense (Clauset et al., 2009). Therefore, we prefer Mc = 0.9, a more conservative value for the magnitude of completeness to show the stability of our later analysis (see Text S1 in Supporting Information S1 for more details). Our catalog presents a decrease in the magnitude of completeness compared to the Mc = 1.8 derived for Vuan et al. (2018) and the template's catalog, considering the same estimation described above.

This new catalog is the largest catalog for this precursory sequence to date (Sugan et al. [2014] reported 3571 events and Vuan et al. [2018] extended using one station up to 3786 events), and is created using many constraints to ensure high quality of the detections, such as the selection of the templates based on the SNR criteria for P and S waves, a higher frequency band, an N-value threshold selection determined from non-physical acausal

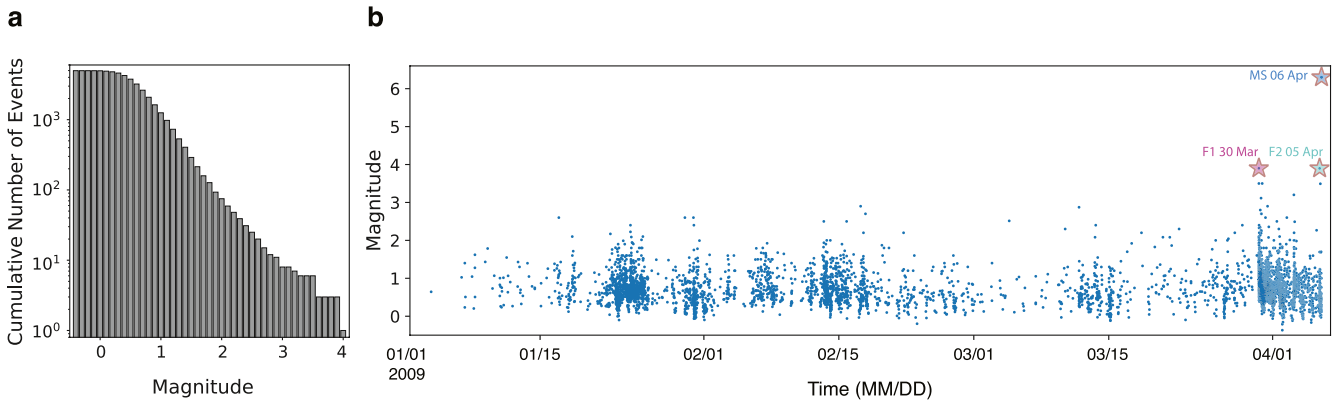

Figure 2. (a) Magnitude-frequency distribution (0.1 bin) for events detected. (b) Estimated magnitudes (see "Extending the Seismic Catalog" section for more details).

templates, a relocation to measure the distance between templates and detections, and a longer period of time scanned.

Figure 3a shows that the seismicity starts on January 3 and lasts until April 6, when the mainshock occurs on the main fault. No seismicity is detected in the period between 6 October 2008–2 January 2009, so we consider the seismicity starting on the 3 of January as foreshocks of the 9 of April Mw 6.1 earthquake (Chiaraluce, Valoroso, et al., 2011; Sugan et al., 2014; Valoroso et al., 2013; Vuan et al., 2018). We observe that the rate of events strongly increases after a Mw 3.9 foreshock on 30 March (F1), which activates an antithetic fault (Chiaraluce, Valoroso, et al., 2011; Valoroso et al., 2013). This activation of the seismicity on the antithetic fault is evidenced in Figure 3b, which shows a summary of the vertical normalized waveforms for the AQU station (the closest one to the mainshock epicenter, see Figure 1) aligned on the P-wave arrival. A significant difference in the S-wave arrivals is observed after F1, at the same time as the spatial evolution reported by Chiaraluce, Valoroso, et al. (2011) and Valoroso et al. (2013) (see also Movie S1). As a first analysis, we split the seismicity before and after F1 on 30 March into two sequences (hereafter S1 and S2, respectively). We observe that the respective cumulative event counts (Figures 3a and 3c) of sequences S1 and S2 exhibit different time evolutions. The seismicity during S1 is characterized by a slow time evolution, with several accelerations occurring over a few days (Figures 2 and 3a and 3c) and without any clear mainshock driving them (Figure 2b). On the other hand, the cumulative number of events in S2 evolves with a log-like behavior similar to an aftershock Omori law (Utsu & Ogata, 1995).

We track the spatio-temporal evolution of several parameters that describe the style of the seismicity and provide hints about the physical processes active during the foreshock sequence. The mainshock is excluded from this analysis.

3. Tracking Foreshocks

We study and discuss the spatio-temporal evolution of the seismicity by tracking the time development of several parameters that characterize the style of seismicity. The parameters are estimated using moving windows of 100-events with a 99-events overlap, that is, the first estimate considers the first 100-events, and each subsequent estimate is just shifted by one event in time. This approach allows us to characterize the general evolution of the sequence rather than just focusing on specific time periods. At this point, it is necessary to consider the potential effects of the magnitude of completeness and the number of events used in each time window. To that scope, we performed tests considering only events with magnitudes larger than the magnitude of completeness and assessed the effect of varying numbers of events for windows-lengths and overlaps, to evaluate the stability of the results (see Figure S7-10 in Supporting Information S1). A jack-knife process was also carried out, removing 20% of the catalog in 100 realizations, to assess the uncertainties for each parameter (Figure S7-10 in Supporting Information S1). Considering the robustness of the tests mentioned above, we present here the results for the entire catalog (Figures 4–6).

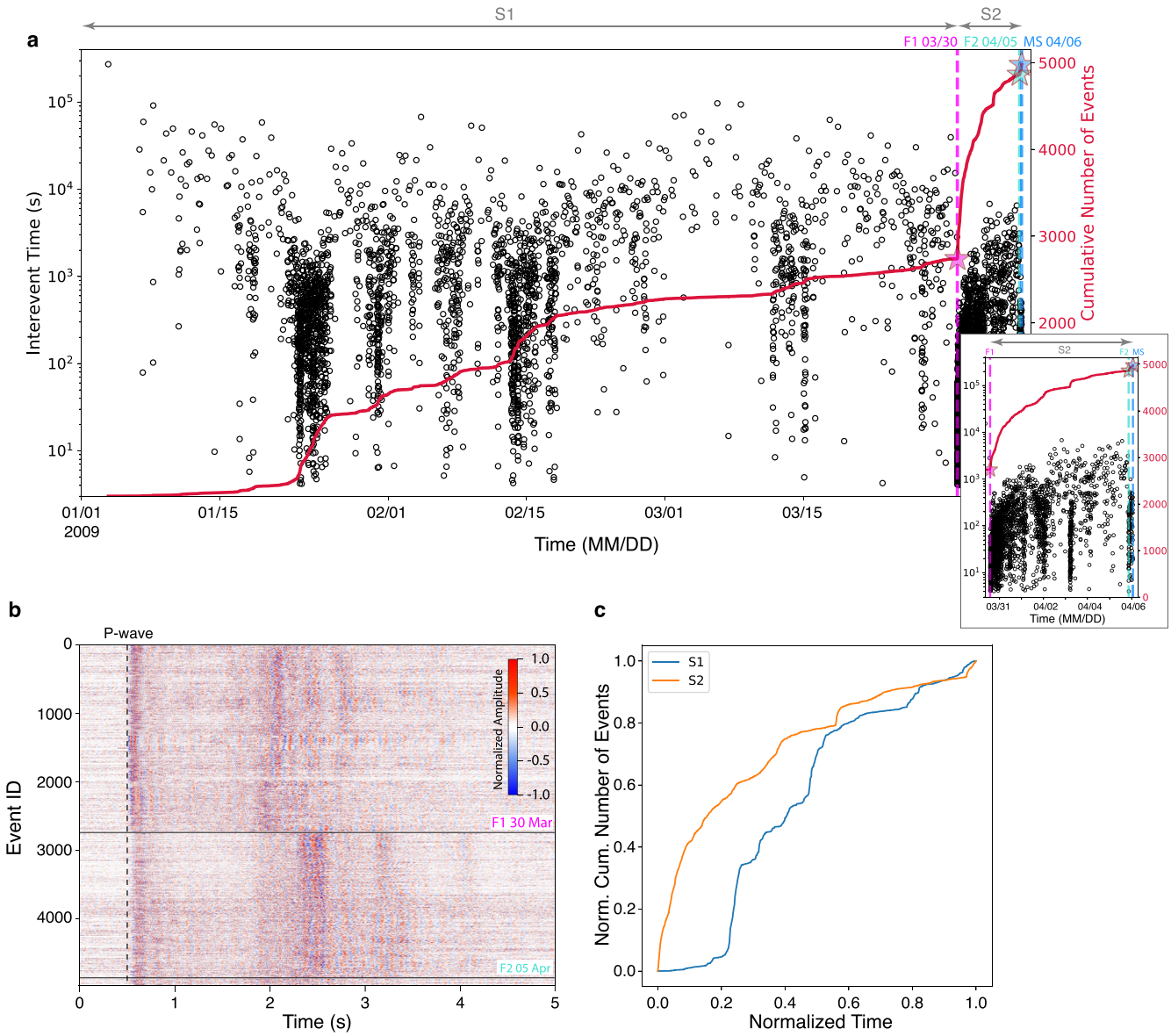

Figure 3. Catalog generated using template matching. (a) Interevent times are plotted using black circles, defined as the elapsed time between consecutive events. Red line represents the cumulative number of events, and magenta, cyan, and blue vertical lines show the time of F1, F2, and mainshock (MS) events, respectively. Inset: a zoom of the time interval between F1 and the mainshock. (b) Normalized waveforms of the catalog for the vertical component of the AQU station, aligned 0.5 s before estimated P-wave arrival (black vertical dashed line). Event ID is chronologically ordered (i.e., the vertical axis is time-ordered). Time of occurrence of F1 and F2 are also indicated with black horizontal lines. (c) Comparison between the normalized cumulative event count for S1 and S2.

3.1. Temporal Clustering

Temporal clustering of seismicity, that is, how past events affect the occurrence of the future ones, is a key feature of seismicity and is thought to be principally related to static or dynamic stress transfer (Freed, 2005). Therefore, the study of temporal clustering probes the degree to which earthquake interactions drive the propagation of seismic sequences over external forcing or other physical processes (Schoenball & Ellsworth, 2017).

To quantify the level of time clustering of the seismicity, we estimate the coefficient of variation (COV) of the interevent times (τ) (Figure 3a) as $COV(\tau) = \sigma_\tau / \bar{\tau}$, where σ_τ is the standard deviation and $\bar{\tau}$ is the average of the interevent times within the window (Kagan & Jackson, 1991). The COV is 0 for a periodic occurrence of seismicity, 1 for completely random Poisson occurrence, and larger than 1 for temporally clustered earthquakes;

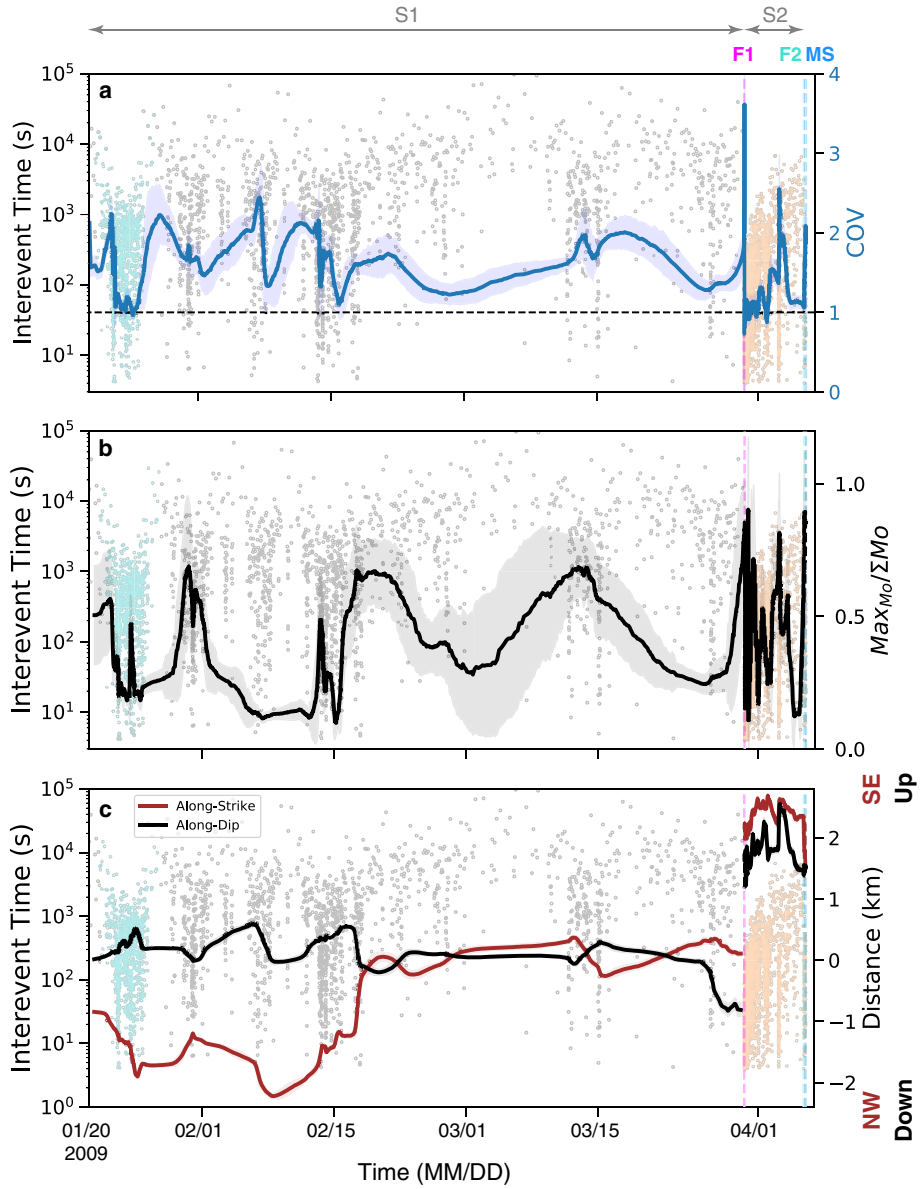

Figure 4. Temporal evolution with a sliding 100-event window length and a 99-event overlap for: (a) Coefficient of variation of the interevent times (b) Ratio between the maximum value of Mo and its total amount within the window (c) Average along-strike and along-dip location of the seismicity measured relative to the mainshock (MS) and projected on the main fault. Time corresponds to the time of the last event within the 100-event window (see text). Interevent times plotted in Figure 3a is also indicated in Figures a, b and c (gray dots). Magenta, cyan, and blue vertical dashed lines show the time of F1, F2, and MS events, respectively. Cyan and light orange dots represent zoom in presented in Figure 5.

put plainly, the larger the COV is, the stronger the time clustering is (Kagan & Jackson, 1991; Sánchez-Reyes et al., 2021; Schoenball & Ellsworth, 2017).

Figure 4a shows the temporal evolution of the COV. During S1 we see slow oscillations of the COV, with generally low values (ranging from 1 to 2.5). We observe that decreases of the COV are often associated with accelerations of seismicity (Figure 4a). The lowest values (COV ~ 1) for S1 are observed during an increases of the seismicity rate starting on 21 January (cyan dots in Figure 4a) and on ~15 February. This observation suggests that the increment of seismicity rate is not due to interevent stress triggering (e.g., seismicity is not driven by a mainshock), and an external mechanism likely acts to increase the number of events (Beaucé et al., 2019). On the other hand, periods with increased seismicity rates within S2 exhibit episodic, strong temporal clustering followed by random

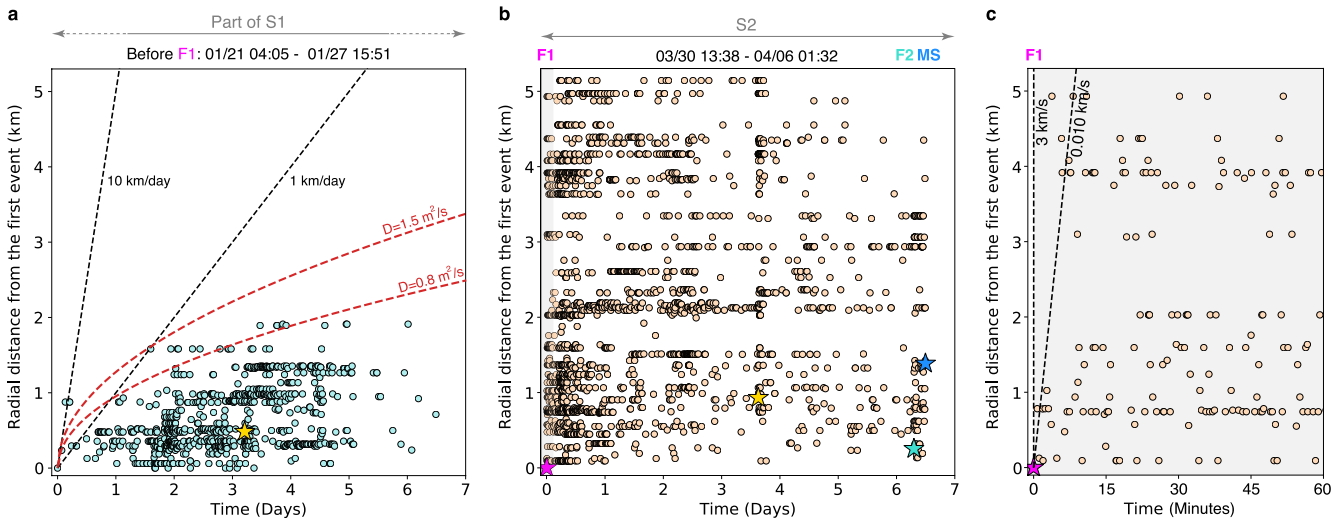

Figure 5. (a) Example of radial spatial migration (measured from the first event of the sequence) for a burst during S1 (see Figure 4). Yellow star represents the largest event within the sequence (M2.4 according to Chiaraluce, Valoroso, et al., 2011). Red dashed lines represent best-fit fluid diffusion curves (Shapiro et al., 1997) for hydraulic diffusivity of 1.5 m2/s (all the seismicity in a) and 0.8 m^2/s (95-percentile of the seismicity in (a). (b) Example of radial spatial migration for S2 (see Figure 4). Magenta, cyan, and blue vertical stars show the time of F1, F2, and mainshock events, respectively, and yellow star represent another event magnitude 3.2 in the middle of the sequence. (c) Zoom for the first 60 min plotted in (b).

seismicity akin to mainshock-aftershock sequences (Schoenball & Ellsworth, 2017). Summarizing, the COV evolution reflects changes in the seismicity style as a function of time, especially when moving from S1 to S2.

3.2. Evolution of Seismic Moment Release

The time evolution of the seismic moment (Mo) release reflects the behavior of different types of seismic sequences and offers insights into the processes on activated faults (Vidale & Shearer, 2006). While a stable and gradual moment release by many earthquakes without a dominant large magnitude event is observed for swarm-type sequences (Vidale & Shearer, 2006), most of the moment is released at once during mainshock-aftershocks sequences (Mogi, 1963).

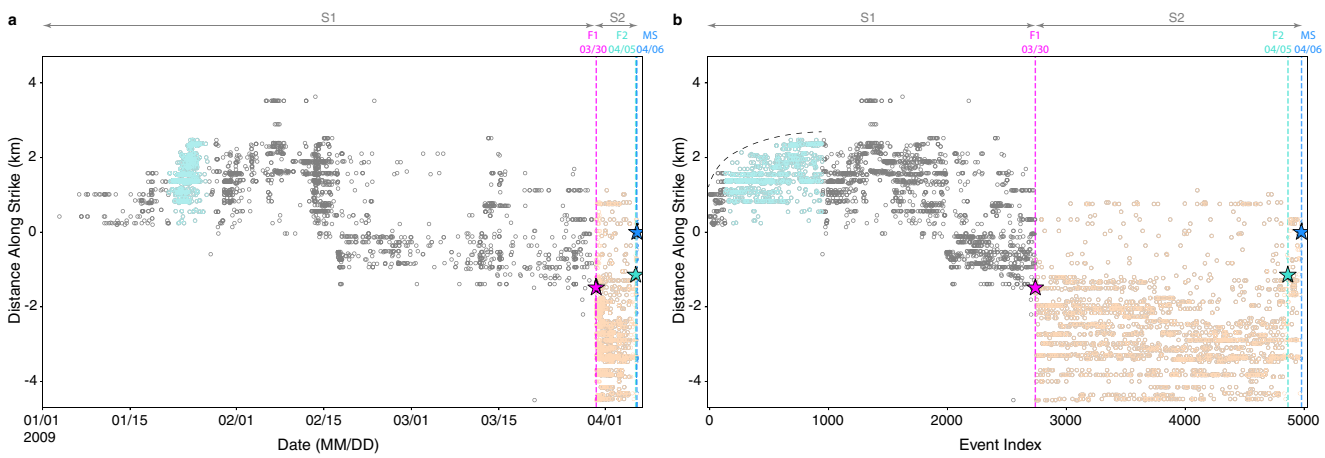

Figure 6. Along-strike distribution of the seismicity centered in the mainshock for (a) time plot and (b) event-index plot. The groups of seismicity are shown in Figure 5a are highlighted in cyan (part of S1) and light orange (S2). Magenta, cyan, and blue vertical lines with stars show the time of F1, F2, and mainshock (MS) events, respectively. Note that the strike considered is the one of the main faults N133°E (Valoroso et al., 2013).

To analyze the time evolution of the seismic moment release, we estimate for each 100-event sliding window the ratio of the maximum seismic moment to the total seismic moment of the window (MaxMo/$\sum Mo$, see Figure 4b). Values close to 1 indicate episodes when the largest event represents most of the Mo released, whereas values close to 0 are observed for windows without a dominant event in terms of moment release. We estimate the moment for each event using the definition of Mw of Kanamori (1977).

Our analysis shows a smooth evolution of the moment ratio during S1 (Figure 4b), with values ranging from 0.1 to 0.6. This implies that the seismic moment is released nearly uniformly within the window, rather than impulsively by some dominant event. From the beginning of the sequence until 15 February, the moment ratio is generally low, despite some periods with increased seismicity rates when larger events occur (Figure 4b). From 15 February until F1 we observe an increase of the moment ratio associated with larger events M2.7 and M 2.9 (17 February and 11 March, respectively; see Figures 2a and 4b). During S2, the evolution of moment release is more episodic, with large rapid releases of the moment, mainly associated with the largest foreshocks (e.g., F1 and F2). A comparison of Figures 4a and 4b shows that the COV and seismic moment release have similar patterns, especially during S2, with peak values associated with the largest foreshocks followed by a rapid decrease of COV and moment release. We note that for the moment ratio, the size of the selected window has an effect on the observed level of smoothing; the maximum magnitude (numerator) does not change with different window sizes while the total moment (denominator) does. We observe that smaller windows increase the relative values of small mainshock-aftershocks sequences (e.g., Figure S9 in Supporting Information S1), which makes the evolution of the moment ratio more episodic and less smooth; this effect is diminished for larger windows (e.g., Figure S10 in Supporting Information S1).

3.3. Spatial Evolution

To assess the spatial evolution of the seismicity as a function of time we track the along-strike and along-dip position of the events. We first project all the seismicity onto the main fault plane for S1 (strike N133°E and Dip 50° according to Valoroso et al. [2013]) and an orthogonal fault plane for S2 (when the antithetic fault is active), obtaining along-strike and along-dip distances measured from the position of the mainshock. We thus track the position of the seismicity centroid (estimated as the average of all event locations) for each time window and extract the along-strike and along-dip coordinates, which are plotted in Figure 4c. In addition, the 3D evolution is presented in the supplementary material (see Movie S1).

As previously observed by Sugan et al. (2014), the seismicity starts on the north-west segment of the fault (Figure 4c). We observe a slow but significant movement of the centroid along strike and dip until 13 February, mainly during increases of the seismicity rate. Observations along with the 3D spatial evolution presented in Movie S1 suggest seismicity re-ruptures the same fault segment. After the initial activity in the NW segment of the fault, a prominent along-strike migration occurs toward the south-east, observed in Movie S1 and also tracked by the large along-strike variation of the centroid (Figure 4c). This migration begins around 13 February, accelerates on 17 February covering ∼1.2 km in less than 24 hr, and fades on 18 February. At this point, the along-dip and along-strike position of the seismicity stabilizes until the end of S1. An example of the seismicity migratory behavior within S1 is shown in Figure 5a (group of cyan dots in Figure 4). On 21 January 2009, velocities of kilometers per day are required to reproduce the seismicity front (we discuss this in more detail in Section 4).

During the second sequence S2 the antithetic fault is activated after foreshock F1, and Figure 4c shows that the centroid of the seismicity is confined between 1.5 and 2.5 km from the hypocenter both along dip and strike. In addition, the 3D evolution of the seismicity during S2 (Movie S1) does not exhibit slow migrations as observed in S1, but rather a rapid spread of the seismicity across the antithetic fault. This latter behavior is exemplified by Figures 5b and 5c, with longer distances (kilometers) rapidly covered in seconds by seismicity after the occurrence of major events (e.g., F1, F2, and another event magnitude 3.2 in the middle of the sequence indicated by a yellow star). These distances are longer than the expected magnitude-dependent rupture lengths of the major earthquakes which are about ∼400–800 m for a M3.9 event (e.g., Dascher-Cousineau et al., 2020; Udias et al., 2014). The strong clustering that we observe in the COV (Figure 4a) at the moment of large foreshocks in S2 (e.g., F2) together with the rapid large scale spreading of the seismicity (Vel. = 3 km/s), suggests that stress triggering is the main mechanism driving the seismicity during the bursts in S2 (Freed, 2005).

3.4. Event Index Evolution of the Sequence

The migration style of earthquake locations is generally considered to be an important characteristic to distinguish earthquake swarms from aftershock sequences (Fischer & Hainzl, 2021). While swarms typically show hypocenter migration that depends on the mechanism driving the swarm (e.g., pore-pressure diffusion, Shapiro et al. [1997]; hydraulic fracture growth, Dahm et al. [2010]; or slow slip, Schwartz & Rokosky [2007]), aftershocks usually occur immediately across the entire fault plane and along the edges of the mainshock rupture due to stress transfer (e.g., Freed, 2005) although some slower migrations can be linked to afterslip (e.g., Perfettini et al., 2018). Usually, the way to analyze such migration patterns is in the distance-time domain, where the independent variable is typically the time. However, as shown by Fischer and Hainzl (2021) a complimentary analysis tool is to use the event order (e.g., event index) as the independent variable, which is also termed natural time (Rundle et al., 2018). While the use of time as an independent variable allows resolving whether time controls the seismogenic process, the use of the event index indicates whether the seismogenic process itself controls the seismicity, that is, whether each rupture facilitates the nucleation of the next rupture (Fischer & Hainzl, 2021). Fischer and Hainzl (2021) showed that an index-plot migration is linear or square-root for either external processes such as pore-pressure diffusion, hydraulic fracture, and slow slip or in case of an internal process, such as the creation of pore-space during ruptures. In contrast to the random (in space) occurrence of aftershock hypocenters along the mainshock fault plane.

Figure 6 shows the comparison between the time (Figure 6a) and the event-index (Figure 6b) plots for the along-strike position of the seismicity, centered in the mainshock. We observe a coherent spreading of seismicity during S1 (e.g., Figure 6 a and b, cyan dots), suggesting that the active area is increasing due to the occurrence of an external seismicity mechanism. On the other hand, during S2 (Figure 6 a and b, light orange dots) the event-index plot does not show any migration, even after removing the time dependence. Instead, we observe a continuous occurrence of events likely resulting from stress transfer, for which no migration patterns are expected (Figure 6b; Helmstetter and Sornette [2002]).

3.5. Effective Stress Drop

We further track the temporal evolution of the effective stress drop ($\Delta\sigma_{eff}$) measured by comparing the cumulative seismic moment and the areal extent of the sequence (Fischer & Hainzl, 2017; Roland & McGuire, 2009). The region enclosing the seismic events was measured using a Delaunay triangulation, after projecting all the seismicity onto the main fault plane for S1 (strike N133° and dip 50° according to Valoroso et al. [2013]) and an orthogonal fault plane for S2 (where the antithetic fault is active). An example of this process is shown in Figure S11 in Supporting Information S1. Following Fischer and Hainzl (2017), we impose a distance threshold between neighboring events to avoid outliers, with a maximum triangle leg length of 2.5 km according to the size of the hypocenter cloud. Similar to the previous analysis, the initial window contains 100 events to estimate the rupture area and the cumulative seismic moment $\left(\sum M_o\right)$. We then accumulate event by event, and for each window, we derive the effective stress drop as $\Delta\sigma_{eff} = \frac{7}{16}\frac{\sum M_o}{r^3}$ (Fischer & Hainzl, 2017). r is here the radius of an assumed circle with the same area as estimated from the triangulation. This procedure was carried out individually for each fault, and their respective results are plotted in Figure 7.

During S1, we observe a rapid increase in both the radius (the region enclosing seismicity) and the cumulative seismic moment (Figure 7a) until about 25 January. Then, both parameters become more stable until F1. The first part (S1) of the sequence releases a total seismic moment of 2.9 x 10^{14} Nm (~Mw 3.6, without considering F1). The behavior of S2 is different: both $\sum M_o$ and r rapidly grow, reaching a radius and cumulative seismic moment greater than the values during S1 in a shorter time. Figure 7b shows the time evolution of the effective stress drop for both S1 and S2. The comparison between the effective stress drops for S1 and S2 highlights that during S1, the seismicity takes place over a wider area than the area of released seismic moment (Fischer & Hainzl, 2017). This leads to a lower effective stress drop of ~0.01 MPa for S1. Whereas in S2, the higher effective stress drop (~0.1 MPa) indicates that most of the area enclosing the seismicity is seismically active. These values are of the order of effective stress drops estimated by Roland and McGuire (2009) for seismic swarms along Southern California and the East Pacific Rise transform faults. In addition, the difference of almost one order of magnitude between S1 and S2 is similar to differences in the effective stress drop observed by Fischer and Hainzl (2017) for different seismic sequences such as injection-induced seismicity, natural earthquake swarms,

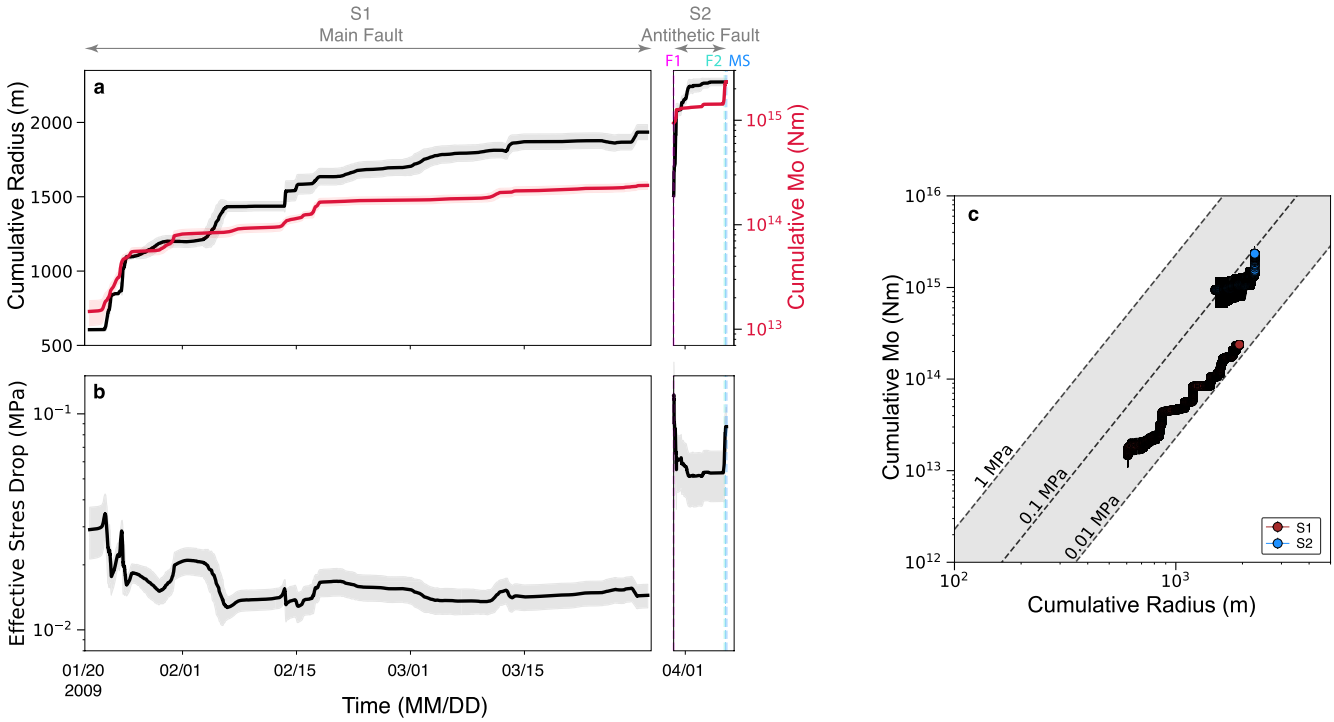

Figure 7. Cumulated moment, radius, and effective stress drop evolution. We use 100-events windows-length and 99 events overlapping for (a) cumulated radius (black line) and cumulated moment (red line). (b) Effective stress drop. Time corresponds to the time of the last event within the 100-events window (see text). (c) Scaling between the cumulated radius and cumulated moment for the first part of the sequence (S1, red dots) and the second part (S2, blue dots).

and mainshock-aftershock sequences. In addition, we analyze the cumulative radius as a function of cumulative M_o (Figure 7c). We observe that our measurements are characterized by a cubic scaling of the seismic moment with earthquake cluster radius ($M_o \propto r^3$) but for different constant stress drops. Such scaling is predicted in the case of fault models with brittle or mixed (brittle and ductile) rheology and homogeneous prestress (Fischer & Hainzl, 2017). According to Fischer and Hainzl (2017), the scaling together with effective stress differences can be used to discriminate different physical processes driving a seismic sequence.

4. Discussions

The analysis of the seismicity preceding the Mw 6.1 L'Aquila earthquake reveals a sudden increase of earthquake activity in January 2009, ~3 months prior to the mainshock (Figure 2a). From the beginning of the seismicity to the mainshock, almost 5000 foreshocks released a seismic moment of ~3 x 10^{15} Nm (~Mw 4.3, Figure 7a). Based on our estimated parameters (Section 3), we observe that the foreshocks sequence develops in two distinct phases and features a complex spatio-temporal evolution. The two stages of behavior that we report (mostly aseismic, S1, then mostly seismic, S2) has been observed in several other studies, in different tectonic settings (e.g., Durand et al., 2020; Kato et al., 2012; Ruiz et al., 2017, 2014; Socquet et al., 2017).

The first part of the sequence (S1) is characterized by a relatively low temporal interaction of the seismicity (Figure 4a), smooth moment release (Figure 4b), and a slow but significant movement of the centroid of the seismicity (Figure 4c). We also observe migrations lasting up to 7 days (Figures 5a and Figure 6). The linear velocity of these migrations ranges from 1 to 10 km/day (Figure 5a); these velocities are similar to those associated with seismic swarms driven by aseismic slip (e.g., De Barros et al., 2020). Finally, we observe migrations in time-space and event-index-space (Figure 6), which is indicative that an external seismogenic process controls the seismicity (Fischer & Hainzl, 2021).

If seismicity is a byproduct of aseismic slip, its intermittent time evolution (Figure 3a) reflects a variable rate of aseismic slip during the first part of the sequence. Similar behavior is observed during slow slips in subductions

zones, with bursts of aseismic slips mainly occurring in rapid episodes associated with bursts of tremors and/or low frequency earthquakes (e.g., Jolivet & Frank, 2020; Rousset et al., 2019). However, confirming the existence of aseismic slip using independent data as GNSS is difficult, as the expected surface displacement expected during the bursts of seismicity is smaller than the environmental signals often observed in GNSS data along the Apennines (Amoruso et al., 2017). For example, Borghi et al. (2016) proposed that a slow slip event started the 12 February and lasted for almost 2 weeks. However, Amoruso et al. (2017) showed that this signal was due to environmental noise likely caused by temperature and precipitation.

The observed migrations (Figure 5a) may also be explained by fluid diffusion (Shapiro et al., 1997; e.g., Ruhl et al., 2016), considering hydraulic diffusivities of 0.8 and 1.5 m^2/s, which are within expected values for the crust (Scholz, 2019; Talwani & Acree, 1985). If this was the case, it would be in agreement with the significant role of fluids reported in the region by several authors (e.g., Antonioli et al., 2005; Lucente et al., 2010; Poli et al., 2020; Savage, 2010; Terakawa et al., 2010).

The second part of the sequence (S2) starts with a magnitude 3.9 event (F1) on the 30 of March 2009, activating an antithetic fault (Chiaraluce, Valoroso, et al., 2011; Valoroso et al., 2013) similarly to other recent normal fault earthquakes in the region (e.g., Sánchez-Reyes et al., 2021). The activation of several faults highlights that the precursory process for this event is a complex volumetric process (Ben-Zion & Zaliapin, 2020; Savage et al., 2017), and is not limited to the fault plane. S2 is characterized by a high temporal clustering (Figure 4a) and large moment release (Figure 4b). These parameters suggest a strong interaction between seismic events, likely governed by stress triggering (Freed, 2005). No migration is inferred from the event-index analysis (Figure 6), and the speed at which seismicity spreads in time is significantly different from that observed during S1. Figures 5b and 5c show that after F1, the seismicity covers distances of kilometers in seconds to minutes and similar patterns are observed after the occurrence of another magnitude 3.2 events in the middle of S2 (yellow star in Figure 5b) and after F2. These velocities are not compatible with mechanisms such as fluid diffusion or aseismic slip, but rather are likely governed by static or dynamic stress transfer (Freed, 2005).

The respective effective stress drops estimated for S1 and S2 are on the order of 0.01 and 0.1 MPa (Figure 7b). These values are in agreement with estimations in other seismotectonic contexts (e.g., Fischer & Hainzl, 2017; Roland & McGuire, 2009; Schoenball & Ellsworth, 2017), and the difference of $\Delta\sigma_{eff}$ between S1 and S2 (Figure 7b) provides new insights about the physical mechanisms that might take place during the precursory phase of the studied earthquake. Fischer and Hainzl (2017) estimated the effective stress drops for several seismic sequences to be in a range from 8×10^{-5} to 3 MPa. They showed that some sequences such as hydraulic stimulations of geothermal reservoirs, seismic swarms, and mainshock–aftershock-type are associated with effective stress drops from 0.1 to 3.0 MPa, while smaller values (from 8×10^{-5} to 0.018 MPa) correspond to sequences that point to a dominating aseismic deformation (e.g., hydraulic fracturing). Considering the above classification, the low effective stress drop (~0.01 MPa) of S1 (Figure 7b) suggests a dominant role of aseismic deformation during the first part of the sequence, with seismicity occurring over a large area with only a small fraction of the area occupied by asperities releasing seismic energy. In this model, aseismic slip is the main mechanism triggering the activation of distant asperities (Fischer & Hainzl, 2017). Following the models proposed by Fischer and Hainzl (2017), we define S1 as a 'mixed' model, as it implies a fault with low asperity density embedded in a ductile matrix. On the other hand, the larger effective stress drops up to ~0.1 MPa after F1 (Figure 7b) indicates that most of the area enclosing the seismicity is seismically active. In this case, the proximity of asperities favors the stress triggering as a mechanism for time clustering of events (Figure 4a) over short time scales (Figures 5b and 5c). Given these properties, we call this second model 'brittle'.

Both S1 and S2 show a similar cumulative moment versus radius scaling ($M_o \propto r^3$). This scaling is observed either in the case of brittle fault rheology or in the mixed fault rheology models with homogeneous pre-stress, but with the different values of stress drop discussed above (Fischer & Hainzl, 2017). However, in the case of a partly ductile fault with heterogeneous pre-stress, the seismic moment only scales with the square of the radius $M_o \propto r^2$, which is not consistent with our observations (Fischer & Hainzl, 2017, Figure 7c). Considering that the mixed model is representative of S1, and the brittle model of S2 due to the variations of the effective stress drop (Figure 7c), we discuss possible differences between the fault rheologies in S1 and S2.

In the case of brittle asperities embedded in a ductile environment (mixed model during S1), numerical simulations suggest that two scenarios might occur. Either the asperities rupture simultaneously as a single earthquake

or separately as individual events, depending on the distance between the asperities and the frictional strength of the ductile region (Dublanchet et al., 2013; Kaneko et al., 2010; Yabe & Ide, 2017). Thus, high density of the asperities and/or a small $a - b$ frictional parameter in the ductile region lead to simultaneous ruptures of the asperities, while a lower asperity density leads to isolated ruptures, producing a sequence of ruptures with diminished time interaction between each other (Dublanchet et al., 2013; Kaneko et al., 2010; Yabe & Ide, 2017). During S1, the low effective stress drop (Figure 7b) is resulting from void fault areas deformed aseismically among adjacent ruptures, which did not contribute to the seismic moment release (Fischer & Hainzl, 2017, 2021). In this scenario, the existence of large inter-asperities distances is also consistent with the low level of interaction between seismic events inferred from the COV values (Figure 4a)

For the case of brittle fault rheology (S2), the fault segment consists of densely distributed asperities that can rupture individually (Fischer & Hainzl, 2017). For this, some mechanism that prevents the simultaneous rupture of the entire segment and leads to a piecewise rupturing of the fault segment by numerous small earthquakes is needed. Following Yamashita (1999) and Aki and Richards (2002), possible mechanisms might be the presence of barriers, non-stationary loading, or dilatancy due to pore creation, a process suggested by Lucente et al. (2010) after the activation of F1. In this model, due to the proximity between asperities, elastic stress plays an important role during the rupture process. This corresponds closely to what our observations indicate during S2: larger COV values (Figure 4a) imply episodic and rapid releases of the seismic moment (Figure 4b) and seismicity covering larger distances of kilometers in a short time from seconds to minutes (Figures 5b and 5c).

The observed cubic scaling between the accumulated seismic moment and radius is also indicative of re-rupturing for the two models mentioned above (Fischer & Hainzl, 2017). The re-rupturing implies significant overlap between regions hosting subsequent seismic events. This behavior is observed during S1, as reactivation of earthquake families during multiple accelerations of seismicity (Figure 4c, Movie S1, Figure S12 in Supporting Information S1).

The models of Fischer and Hainzl (2017) suggest that the rerupturing process is expected to continue until the stress is fully released within the whole fault segment. Interestingly, although the seismicity of S1 occurs on the fault plane that slipped during the mainshock (Chiaraluce, Valoroso, et al., 2011), there is no overlap between the coseismic slip and the foreshocks (Valoroso et al., 2013, Figure S13 in Supporting Information S1). This suggests that this part of the fault released the full stress in an intermittent fashion through foreshocks (Figure 4b), as the localized fault properties prohibit the nucleation of a large slip episode. Similar behavior has been observed in modelling, where small events appear at the transition from the locked to creeping behavior toward the bottom of the seismogenic zone with decreasing values of the characteristic slip distance of the friction law (Lapusta & Rice, 2003).

5. Conclusion

The analysis of our high-resolution seismic catalog highlights different physical mechanisms that each played a role during the precursory phase of the L'Aquila earthquake. Our results demonstrate how the faults involved in the sequence present quantitative differences in the earthquake activity they host. While the seismicity occurring on the main fault up to 1 week before the mainshock (S1) exhibits minimal time clustering, a smooth moment release, slow migrations, and a lower effective stress drop, the seismicity occurring on the antithetic fault after F1 (S2) shows strong episodic clustering and moment release, a rapid spreading of the seismicity and larger effective stress drop. Such differences in the seismicity behavior indicate that while an external process (aseismic or fluid diffusion, or likely a combination of both) is driving the seismicity in S1, stress transfer is the dominant mechanism during S2. A comparison of our observations with recent seismic swarm models (Fischer & Hainzl, 2017) indicates that during S1 a mixed rheology model of sparse brittle asperities embedded in a ductile environment is likely. On the other hand, brittle fault rheology with a dense population of asperities and small inter-asperity distances is more plausible for the antithetic fault during S2.

Our study shows a complex coalescence of different physical processes occurring during the precursory phase of a large earthquake. Moreover, we highlight how the quantitative analysis of spatio-temporal evolution of microseismicity can unveil complex precursory behaviors, which differ from nucleation models based on simple planar

faults models (Dieterich, 1992; Liu & Rice, 2005; Marone, 1998; Rubin & Ampuero, 2005) aiming for more complex scenarios (e.g., Dutta et al., 2021; Shimizu et al., 2021; Zhang et al., 2014).

Data Availability Statement

Data was downloaded from the Istituto Nazionale di Geofisica e Vulcanologia (INGV, 2006) using obspyDMT (https://github.com/kasra-hosseini/obspyDMT, Hosseini & Sigloch, 2017). The fast matched filter (Beaucé et al., 2018) used in this study can be found at https://github.com/beridel/fast_matched_filter. Computations were performed using the University of Grenoble Alpes (UGA) High-Performance Computing infrastructures CIMENT (https://ciment.univ-grenoble-alpes.fr/wiki-pub/index.php/Welcome_to_the_CIMENT_site!). The catalog generated here is available at https://doi.org/10.5281/zenodo.4776701 (last accessed 20 May 2021).

Acknowledgments
LC and PP were supported by the European Union Horizon 2020 Research and Innovation Programme (grant agreements, 802777-MONIFAULTS). WBF acknowledges support from the National Science Foundation under award EAR-2103408. LC, PP, and WBF were also supported by the Thomas Jefferson Fund award #093. We thank the editor Rachel Abercrombie, the associate editor, and Alessandro Vuan and an anonymous reviewer for their comments that improved our manuscript.

References

Acosta, M., Passelègue, F. X., Schubnel, A., Madariaga, R., & Violay, M. (2019). Can precursory moment release scale with earthquake magnitude? A view from the laboratory. *Geophysical Research Letters*, *46*(22), 12927–12937.

Aki, K., & Richards, P. G. (2002). *Quantitative Seismology* (2nd ed., p. 574). University Science Books.

Amoruso, A., Crescentini, L., & Chiaraluce, L. (2017). Surface temperature and precipitation affecting GPS signals before the 2009 L'Aquila earthquake (Central Italy). *Geophysical Journal International*, *210*(2), 911–918.

Antonioli, A., Piccinini, D., Chiaraluce, L., & Cocco, M. (2005). Fluid flow and seismicity pattern: Evidence from the 1997 Umbria-Marche (central Italy) seismic sequence. *Geophysical Research Letters*, *32*(10), L10311.

Beaucé, E., Frank, W. B., Paul, A., Campillo, M., & van der Hilst, R. D. (2019). Systematic detection of clustered seismicity beneath the Southwestern Alps. *Journal of Geophysical Research: Solid Earth*, *124*(11), 11531–11548.

Beaucé, E., Frank, W. B., & Romanenko, A. (2018). Fast matched filter (FMF): An efficient seismic matched-filter search for both CPU and GPU architectures. *Seismological Research Letters*, *89*(1), 165–172.

Ben-Zion, Y., & Zaliapin, I. (2020). Localization and coalescence of seismicity before large earthquakes. *Geophysical Journal International*, *223*(1), 561–583.

Boncio, P., Pizzi, A., Brozzetti, F., Pomposo, G., Lavecchia, G., Di Naccio, D., & Ferrarini, F. (2010). Coseismic ground deformation of the 6 April 2009 L'Aquila earthquake (central Italy, Mw6. 3). *Geophysical Research Letters*, *37*(6), L06308.

Borghi, A., Aoudia, A., Javed, F., & Barzaghi, R. (2016). Precursory slow-slip loaded the 2009 L'Aquila earthquake sequence. *Geophysical Journal International*, *205*(2), 776–784.

Bouchon, M., Durand, V., Marsan, D., Karabulut, H., & Schmittbuhl, J. (2013). The long precursory phase of most large interplate earthquakes. *Nature Geoscience*, *6*(4), 299–302.

Bouchon, M., Karabulut, H., Aktar, M., Özalaybey, S., Schmittbuhl, J., & Bouin, M. P. (2011). Extended nucleation of the 1999 Mw 7.6 Izmit earthquake. *Science*, *331*(6019), 877–880.

Cabrera, L., Ruiz, S., Poli, P., Contreras-Reyes, E., Osses, A., & Mancini, R. (2021). Northern Chile intermediate-depth earthquakes controlled by plate hydration. *Geophysical Journal International*, *226*(1), 78–90. https://doi.org/10.1093/gji/ggaa565

Cheloni, D., D'agostino, N., D'anastasio, E., Avallone, A., Mantenuto, S., Giuliani, R., et al. (2010). Coseismic and initial post-seismic slip of the 2009 M w 6.3 L'Aquila earthquake, Italy, from GPS measurements. *Geophysical Journal International*, *181*(3), 1539–1546.

Chen, X., & Shearer, P. M. (2013). California foreshock sequences suggest aseismic triggering process. *Geophysical Research Letters*, *40*(11), 2602–2607.

Chiaraluce, L., Chiarabba, C., De Gori, P., Di Stefano, R., Improta, L., Piccinini, D., et al. (2011). The 2009 L'Aquila (central Italy) seismic sequence. *Bollettino di Geofisica Teorica ed Applicata*, *52*(3), 367–387. https://doi.org/10.4430/bgta0019

Chiaraluce, L., Valoroso, L., Piccinini, D., Di Stefano, R., & De Gori, P. (2011). The anatomy of the 2009 L'Aquila normal fault system (central Italy) imaged by high resolution foreshock and aftershock locations. *Journal of Geophysical Research: Solid Earth*, *116*(B12), B12311.

Cirella, A., Piatanesi, A., Cocco, M., Tinti, E., Scognamiglio, L., Michelini, A., et al. (2009). Rupture history of the 2009 L'Aquila (Italy) earthquake from non-linear joint inversion of strong motion and GPS data. *Geophysical Research Letters*, *36*(19), L19304.

Cirella, A., Piatanesi, A., Tinti, E., Chini, M., & Cocco, M. (2012). Complexity of the rupture process during the 2009 L'Aquila, Italy, earthquake. *Geophysical Journal International*, *190*(1), 607–621.

Clauset, A., Shalizi, C. R., & Newman, M. E. (2009). Power-law distributions in empirical data. *SIAM Review*, *51*(4), 661–703.

Dahm, T., Hainzl, S., & Fischer, T. (2010). Bidirectional and unidirectional fracture growth during hydrofracturing: Role of driving stress gradients. *Journal of Geophysical Research*, *115*, B12322. https://doi.org/10.1029/2009jb006817

Dascher-Cousineau, K., Brodsky, E. E., Lay, T., & Goebel, T. H. (2020). What controls variations in aftershock productivity? *Journal of Geophysical Research: Solid Earth*, *125*(2), e2019JB018111.

De Barros, L., Cappa, F., Deschamps, A., & Dublanchet, P. (2020). Imbricated aseismic slip and fluid diffusion drive a seismic swarm in the Corinth Gulf, Greece. *Geophysical Research Letters*, *47*(9), e2020GL087142.

Dieterich, J. H. (1992). Earthquake nucleation on faults with rate-and state-dependent strength. *Tectonophysics*, *211*(1–4), 115–134.

Dodge, D. A., Beroza, G. C., & Ellsworth, W. L. (1995). Foreshock sequence of the 1992 Landers, California, earthquake and its implications for earthquake nucleation. *Journal of Geophysical Research: Solid Earth*, *100*(B6), 9865–9880.

Dodge, D. A., Beroza, G. C., & Ellsworth, W. L. (1996). Detailed observations of California foreshock sequences: Implications for the earthquake initiation process. *Journal of Geophysical Research: Solid Earth*, *101*(B10), 22371–22392.

Dublanchet, P., Bernard, P., & Favreau, P. (2013). Interactions and triggering in a 3-D rate-and-state asperity model. *Journal of Geophysical Research: Solid Earth*, *118*, 2225–2245. https://doi.org/10.1002/jgrb.50187

Durand, V., Bentz, S., Kwiatek, G., Dresen, G., Wollin, C., Heidbach, O., et al. (2020). A two-scale preparation phase preceded an M w 5.8 earthquake in the Sea of Marmara Offshore Istanbul, Turkey. *Seismological Society of America*, *91*(6), 3139–3147.

Dutta, R., Jónsson, S., & Vasyura-Bathke, H. (2021). Simultaneous Bayesian estimation of non-planar fault geometry and spatially-variable slip. *Journal of Geophysical Research: Solid Earth*, e2020JB020441.

Ellsworth, W. L., & Beroza, G. C. (1995). Seismic evidence for an earthquake nucleation phase. *Science*, *268*(5212), 851–855.
Ellsworth, W. L., & Bulut, F. (2018). Nucleation of the 1999 Izmit earthquake by a triggered cascade of foreshocks. *Nature Geoscience*, *11*(7), 531–535.
Falcucci, E., Gori, S., Peronace, E., Fubelli, G., Moro, M., Saroli, M., et al. (2009). The Paganica fault and surface coseismic ruptures caused by the 6 April 2009 earthquake (L'Aquila, central Italy). *Seismological Research Letters*, *80*(6), 940–950.
Fischer, T., & Hainzl, S. (2017). Effective stress drop of earthquake clusters. *Bulletin of the Seismological Society of America*, *107*(5), 2247–2257.
Fischer, T., & Hainzl, S. (2021). The growth of earthquake clusters. *Frontiers of Earth Science*, *9*, 79.
Frank, W. B., Poli, P., & Perfettini, H. (2017). Mapping the rheology of the Central Chile subduction zone with aftershocks. *Geophysical Research Letters*, *44*(11), 5374–5382.
Freed, A. M. (2005). Earthquake triggering by static, dynamic, and postseismic stress transfer. *Annual Review of Earth and Planetary Sciences*, *33*, 335–367.
Gardonio, B., Campillo, M., Marsan, D., Lecointre, A., Bouchon, M., & Letort, J. (2019). Seismic activity preceding the 2011 Mw 9.0 Tohoku earthquake, Japan, analyzed with multidimensional template matching. *Journal of Geophysical Research: Solid Earth*, *124*(7), 6815–6831.
Gibbons, S. J., & Ringdal, F. (2006). The detection of low magnitude seismic events using array-based waveform correlation. *Geophysical Journal International*, *165*(1), 149–166.
Helmstetter, A., & Sornette, D. (2002). Diffusion of epicenters of earthquake aftershocks, Omori's law, and generalized continuous-time random walk models. *Physical Review E*, *66*(6), 061104.
Herrmann, M., & Marzocchi, W. (2021). Inconsistencies and lurking pitfalls in the magnitude–frequency distribution of high-resolution earthquake catalogs. *Seismological Society of America*, *92*(2A), 909–922.
Herrmann, R. B., Malagnini, L., & Munafò, I. (2011). Regional moment tensors of the 2009 L'Aquila earthquake sequence. *Bulletin of the Seismological Society of America*, *101*, 975–993.
Hosseini, K., & Sigloch, K. (2017). Obspydmt: A python toolbox for retrieving and processing large seismological data sets. *Solid Earth*, *8*(5), 1047–1070.
INGV Seismological Data Centre. (2006). *Rete Sismica Nazionale (RSN). Istituto Nazionale di Geofisica e Vulcanologia (INGV)*. https://doi.org/10.13127/SD/X0FXNH7QFY
Jolivet, R., & Frank, W. B. (2020). The transient and intermittent nature of slow slip. *AGU Advances*, *1*(1), e2019AV000126.
Kagan, Y. Y., & Jackson, D. D. (1991). Long-term earthquake clustering. *Geophysical Journal International*, *104*(1), 117–133.
Kanamori, H. (1977). The energy release in great earthquakes. *Journal of geophysical research*, *82*(20), 2981–2987.
Kaneko, Y., Avouac, J.-P., & Lapusta, N. (2010). Towards inferring earth- quake patterns from geodetic observations of interseismic coupling. *Nature Geoscience*, *3*, 363–369. https://doi.org/10.1038/NGEO843
Kato, A., & Ben-Zion, Y. (2020). The generation of large earthquakes. *Nature Reviews Earth & Environment*, *2*, 1–14.
Kato, A., Obara, K., Igarashi, T., Tsuruoka, H., Nakagawa, S., & Hirata, N. (2012). Propagation of slow slip leading up to the 2011 Mw 9.0 Tohoku-Oki earthquake. *Science*, *335*(6069), 705–708.
Lapusta, N., & Rice, J. R. (2003). Nucleation and early seismic propagation of small and large events in a crustal earthquake model. *Journal of Geophysical Research: Solid Earth*, *108*(B4), 2205.
Liu, Y., & Rice, J. R. (2005). Aseismic slip transients emerge spontaneously in three-dimensional rate and state modeling of subduction earthquake sequences. *Journal of Geophysical Research: Solid Earth*, *110*(B8), B08307.
Marone, C. (1998). The effect of loading rate on static friction and the rate of fault healing during the earthquake cycle. *Nature*, *391*(6662), 69–72.
McLaskey, G. C. (2019). Earthquake initiation from laboratory observations and implications for foreshocks. *Journal of Geophysical Research: Solid Earth*, *124*(12), 12882–12904.
McLaskey, G. C., & Kilgore, B. D. (2013). Foreshocks during the nucleation of stick-slip instability. *Journal of Geophysical Research: Solid Earth*, *118*(6), 2982–2997.
McLaskey, G. C., & Lockner, D. A. (2014). Preslip and cascade processes initiating laboratory stick slip. *Journal of Geophysical Research: Solid Earth*, *119*(8), 6323–6336.
MedNet Project Partner Institutions. (1990). Mediterranean Very broadband Seismographic network (MedNet). *Istituto Nazionale di Geofisica e Vulcanologia (INGV)*. https://doi.org/10.13127/SD/FBBBTDTD6Q
Meng, H., & Fan, W. (2021). Immediate foreshocks indicating cascading rupture developments for 527 M 0.9 to 5.4 Ridgecrest earthquakes. *Geophysical Research Letters*, *48*(19), e2021GL095704.
Mogi, K. (1963). Some discussions on aftershocks, foreshocks and earthquake swarms: The fracture of a semi-infinite body caused by an inner stress origin and its relation to the earthquake phenomena (third paper). *Bulletin of the Earthquake Research Institute*, *41*(3), 615–658
Omori, F. (1908). On the fore-shocks of earthquakes. *Bulletin of the Imperial Earthquake Investigation Committee*, *2*(2), 89–100.
Peng, Z., & Zhao, P. (2009). Migration of early aftershocks following the 2004 Parkfield earthquake. *Nature Geoscience*, *2*(12), 877–881.
Perfettini, H., Frank, W. B., Marsan, D., & Bouchon, M. (2018). A model of aftershock migration driven by afterslip. *Geophysical Research Letters*, *45*(5), 2283–2293.
Pio Lucente, F., De Gori, P., Margheriti, L., Piccinini, D., Di Bona, M., Chiarabba, C., & Piana Agostinetti, N. (2010). Temporal variation of seismic velocity and anisotropy before the 2009 MW 6.3 L'Aquila earthquake, Italy. *Geology*, *38*(11), 1015–1018.
Poli, P., Marguin, V., Wang, Q., D'agostino, N., & Johnson, P. (2020). Seasonal and coseismic velocity variation in the region of L'Aquila from single station measurements and implications for crustal rheology. *Journal of Geophysical Research: Solid Earth*, *125*(7), e2019JB019316.
Roland, E., & McGuire, J. J. (2009). Earthquake swarms on transform faults. *Geophysical Journal International*, *178*(3), 1677–1690.
Ross, Z. E., Trugman, D. T., Hauksson, E., & Shearer, P. M. (2019). Searching for hidden earthquakes in Southern California. *Science*, *364*(6442), 767–771.
Rousset, B., Fu, Y., Bartlow, N., & Bürgmann, R. (2019). Weeks-long and years-long slow slip and tectonic tremor episodes on the south central Alaska megathrust. *Journal of Geophysical Research: Solid Earth*, *124*(12), 13392–13403.
Rubin, A. M., & Ampuero, J. P. (2005). Earthquake nucleation on (aging) rate and state faults. *Journal of Geophysical Research: Solid Earth*, *110*(B11).
Ruhl, C. J., Abercrombie, R. E., Smith, K. D., & Zaliapin, I. (2016). Complex spatiotemporal evolution of the 2008 Mw 4.9 Mogul earthquake swarm (Reno, Nevada): Interplay of fluid and faulting. *Journal of Geophysical Research: Solid Earth*, *121*(11), 8196–8216.
Ruiz, S., Aden-Antoniow, F., Baez, J. C., Otarola, C., Potin, B., Del Campo, F., et al. (2017). Nucleation phase and dynamic inversion of the Mw 6.9 Valparaíso 2017 earthquake in Central Chile. *Geophysical Research Letters*, *44*(20), 10–290.
Ruiz, S., Metois, M., Fuenzalida, A., Ruiz, J., Leyton, F., Grandin, R., et al. (2014). Intense foreshocks and a slow slip event preceded the 2014 Iquique Mw 8.1 earthquake. *Science*, *345*(6201), 1165–1169.

Rundle, J. B., Luginbuhl, M., Giguere, A., & Turcotte, D. L. (2018). Natural time, nowcasting and the physics of earthquakes: Estimation of seismic risk to global megacities. *Pure and Applied Geophysics*, *175*, 647–660. https://doi.org/10.1007/s00024-017-1720-x

Sánchez-Reyes, H., Essing, D., Beaucé, E., & Poli, P. (2021). The Imbricated foreshock and aftershock Activities of the Balsorano (Italy) Mw 4.4 normal fault earthquake and implications for earthquake initiation. *Seismological Society of America*.

Savage, H. M., Keranen, K. M., Schaff, D. P., & Dieck, C. (2017). Possible precursory signals in damage zone foreshocks. *Geophysical Research Letters*, *44*(11), 5411–5417.

Savage, M. K. (2010). The role of fluids in earthquake generation in the 2009 Mw 6.3 L'Aquila, Italy, earthquake and its foreshocks. *Geology*, *38*(11), 1055–1056.

Schoenball, M., & Ellsworth, W. L. (2017). A systematic assessment of the spatiotemporal evolution of fault activation through induced seismicity in Oklahoma and southern Kansas. *Journal of Geophysical Research: Solid Earth*, *122*(12), 10–189.

Scholz, C. H. (2019). *The mechanics of earthquakes and faulting*. Cambridge university press.

Schwartz, S. Y., & Rokosky, J. M. (2007). Slow slip events and seismic tremor at circum-pacific subduction zones. *Reviews in Geophysics*, *45*, 1–32. https://doi.org/10.1029/2006RG000208

Scognamiglio, L., Tinti, E., Michelini, A., Dreger, D. S., Cirella, A., Cocco, M., et al. (2010). Fast determination of moment tensors and rupture history: What has been learned from the 6 April 2009 L'Aquila earthquake sequence. *Seismological Research Letters*, *81*(6), 892–906.

Shapiro, S. A., Huenges, E., & Borm, G. (1997). Estimating the crust permeability from fluid-injection-induced seismic emission at the KTB site. *Geophysical Journal International*, *131*(2), F15–F18.

Shelly, D. R. (2020). A high-resolution seismic catalog for the initial 2019 Ridgecrest earthquake sequence: Foreshocks, aftershocks, and faulting complexity. *Seismological Research Letters*, *91*(4), 1971–1978.

Shimizu, K., Yagi, Y., Okuwaki, R., & Fukahata, Y. (2021). Construction of fault geometry by finite-fault inversion of teleseismic data. *Geophysical Journal International*, *224*(2), 1003–1014.

Simon, V., Kraft, T., Diehl, T., & Tormann, T. (2021). Possible precursory slow-slip to two ML∼ 3 main events of the Diemtigen microearthquake sequence, Switzerland. *Geophysical Research Letters*, *48*(19), e2021GL093783.

Socquet, A., Valdes, J. P., Jara, J., Cotton, F., Walpersdorf, A., Cotte, N., et al. (2017). An 8 month slow slip event triggers progressive nucleation of the 2014 Chile megathrust. *Geophysical Research Letters*, *44*(9), 4046–4053.

Sugan, M., Kato, A., Miyake, H., Nakagawa, S., & Vuan, A. (2014). The preparatory phase of the 2009 Mw 6.3 L'Aquila earthquake by improving the detection capability of low-magnitude foreshocks. *Geophysical Research Letters*, *41*(17), 6137–6144.

Talwani, P., & Acree, S. (1985). Pore pressure diffusion and the mechanism of reservoir-induced seismicity. In *Earthquake prediction* (pp. 947–965).

Tape, C., Holtkamp, S., Silwal, V., Hawthorne, J., Kaneko, Y., Ampuero, J. P., et al. (2018). Earthquake nucleation and fault slip complexity in the lower crust of central Alaska. *Nature Geoscience*, *11*(7), 536–541.

Terakawa, T., Zoporowski, A., Galvan, B., & Miller, S. A. (2010). High-pressure fluid at hypocentral depths in the L'Aquila region inferred from earthquake focal mechanisms. *Geology*, *38*(11), 995–998.

Trugman, D. T., & Shearer, P. M. (2017). GrowClust: A hierarchical clustering algorithm for relative earthquake relocation, with application to the Spanish Springs and Sheldon, Nevada, earthquake sequences. *Seismological Research Letters*, *88*(2A), 379–391.

Udías, A., Vallina, A. U., Madariaga, R., & Buforn, E. (2014). *Source mechanisms of earthquakes: Theory and practice*. Cambridge University Press.

Utsu, T., & Ogata, Y. (1995). The centenary of the Omori formula for a decay law of aftershock activity. *Journal of Physics of the Earth*, *43*(1), 1–33.

Valoroso, L., Chiaraluce, L., Piccinini, D., Di Stefano, R., Schaff, D., & Waldhauser, F. (2013). Radiography of a normal fault system by 64,000 high-precision earthquake locations: The 2009 L'Aquila (central Italy) case study. Journal of Geophysical Research. *Solid Earth*, *118*(3), 1156–1176.

Vidale, J. E., & Shearer, P. M. (2006). A survey of 71 earthquake bursts across southern California: Exploring the role of pore fluid pressure fluctuations and aseismic slip as drivers. *Journal of Geophysical Research: Solid Earth*, *111*(B5), B05312.

Vuan, A., Sugan, M., Amati, G., & Kato, A. (2018). Improving the detection of low-magnitude seismicity preceding the Mw 6.3 L'Aquila earthquake: Development of a scalable code based on the cross correlation of template earthquakes improving the detection of low-magnitude seismicity preceding the Mw 6.3 L'Aquila earthquake. *Bulletin of the Seismological Society of America*, *108*(1), 471–480.

Yabe, S., & Ide, S. (2017). Slip-behavior transitions of a heterogeneous linear fault. *Journal of Geophysical Research: Solid Earth*, *122*, 387–410. https://doi.org/10.1002/2016JB013132

Yamashita, T. (1999). Pore creation due to fault slip in a fluid-permeated fault zone and its effect on seismicity: Mechanism of earthquake swarm. *Pure and Applied Geophysics*, *155*, 625–647.

Yoon, C. E., Yoshimitsu, N., Ellsworth, W. L., & Beroza, G. C. (2019). Foreshocks and mainshock nucleation of the 1999 Mw 7.1 Hector mine, California, earthquake. *Journal of Geophysical Research: Solid Earth*, *124*(2), 1569–1582.

Zhang, Z., Zhang, W., & Chen, X. (2014). Three-dimensional curved grid finite-difference modelling for non-planar rupture dynamics. *Geophysical Journal International*, *199*(2), 860–879.

Reference From the Supporting Information

De Gori, P., Lucente, F. P., Lombardi, A. M., Chiarabba, C., & Montuori, C. (2012). Heterogeneities along the 2009 L'Aquila normal fault inferred by the b-value distribution. *Geophysical Research Letters*, *39*(15).